THE ASTROPHYSICAL JOURNAL, 479:933–947, 1997 April 20


# RAPID SPIN-UP EPISODES IN THE WIND-FED ACCRETING PULSAR GX 301−2

DANNY T. KOH, LARS BILDSTEN,[1] DEEPTO CHAKRABARTY,[2] ROBERT W. NELSON,
THOMAS A. PRINCE, AND BRIAN A. VAUGHAN
Space Radiation Laboratory, California Institute of Technology, Pasadena, CA 91125;
koh@srl.caltech.edu, bildsten@fire.berkeley.edu, deepto@space.mit.edu, nelson@tapir.caltech.edu,
prince@srl.caltech.edu, brian@srl.caltech.edu

AND

MARK H. FINGER,[3] ROBERT B. WILSON, AND BRADLEY C. RUBIN[4]
Space Sciences Laboratory, NASA/Marshall Space Flight Center, Huntsville, AL 35812;
finger@gibson.msfc.nasa.gov, wilson@gibson.msfc.nasa.gov,
rubin@ssl.msfc.nasa.gov
*Received 1996 September 13; accepted 1996 November 13*

## ABSTRACT

The accreting pulsar GX 301−2 ($P = 680$ s) has been observed continuously by the large-area detectors of the Burst and Transient Source Experiment (BATSE) instrument on the *Compton Gamma Ray Observatory* since 1991 April 5. Orbital parameters determined from these data are consistent with previous measurements, with improved accuracy in the current orbital epoch. The most striking features in the pulsar frequency history are two steady and rapid spin-up episodes, with $\dot{\nu} \approx (3\text{–}5) \times 10^{-12}$ Hz s$^{-1}$, each lasting for about 30 days. They probably represent the formation of transient accretion disks in this wind-fed pulsar. Except for these spin-up episodes, there are virtually no net changes in the neutron star spin frequency on long timescales. We suggest that the long-term spin-up trend observed since 1984 ($\dot{\nu} \approx 2 \times 10^{-13}$ Hz s$^{-1}$) may be due entirely to brief ($\approx$20 days) spin-up episodes similar to those we have discovered.

We assess different accretion models and their ability to explain the orbital phase dependence of the observed flux. In addition to the previously observed preperiastron peak at orbital phase $0.956 \pm 0.022$, we also find a smaller peak close to apastron at orbital phase $0.498 \pm 0.057$. We show that if the companion star's effective temperature is less than 22,000 K, then it must have a mass $M_c < 70\ M_\odot$ and a radius $R_c < 85\ R_\odot$ so as not to overfill the tidal lobe at periastron. In order not to overflow the Roche lobe at periastron, the corresponding values are $M_c < 55\ M_\odot$ and $R_c < 68\ R_\odot$. These constraints are nearly at odds with the reclassification by Kaper et al. of the companion as a B1 Ia+ hypergiant.

*Subject headings:* binaries: close — pulsars: individual (GX 301−2) — stars: rotation — X-rays: stars

## 1. INTRODUCTION

An accretion-powered pulsar consists of a rotating magnetized neutron star accreting material transferred from a binary companion. In systems with evolved low-mass companions, mass transfer occurs via Roche lobe overflow and is mediated by an accretion disk. If the companion star has high mass, the neutron star can accrete directly from the stellar wind. One such wind-fed system is GX 301−2 (4U 1223−62), a 680 s accreting pulsar in a 41.5 day eccentric ($e = 0.47$) orbit around the supergiant companion Wray 977 (Sato et al. 1986, hereafter S86). Pulsations of $\approx$700 s were first detected in this binary in 1975 (White et al. 1976). The X-ray mass function is 31.8 $M_\odot$, making the minimum companion mass $\approx$35 $M_\odot$ for a 1.4 $M_\odot$ neutron star. The B2 Iae spectral classification of Wray 977 (Parkes et al. 1980) implies that the star has already evolved off the main sequence and is at least $10^6$ years old.

We have observed GX 301−2 continuously with the BATSE instrument since 1991 April and redetermined independently the binary orbital parameters. These are consistent with S86's measurements, but we have obtained a substantially better measurement of the time of periastron passage. This improvement permits accurate removal of orbital effects from the observed pulsed frequency history, yielding the intrinsic neutron star spin frequency. Figure 1 shows the intrinsic neutron star frequency for the last 20 years. From 1975–1985, the neutron star was, on average, neither spinning up nor down, much like other wind accretors. However, a prolonged period of spin-up at $\dot{\nu} \approx 2 \times 10^{-13}$ Hz s$^{-1}$ began in 1985 roughly.

The neutron star flares regularly in X-rays $\approx$1.4 days before periastron passage (S86), and several stellar wind accretion models have been proposed to explain the magnitude of the flares and their orbital phase dependence (White & Swank 1984; Haberl 1991). In addition to the well-known maximum just before periastron passage, the 20–55 keV BATSE-pulsed flux history folded at the orbital period reveals a secondary maximum close to apastron, which is difficult to explain in a spherically symmetric stellar wind.

We begin in § 2 by discussing the BATSE data used in our analysis and quantifying the enhanced sensitivity obtained by subtracting the *Compton Gamma Ray Observatory* orbital variations from the raw data. The orbit determination and resulting intrinsic spin frequency measurements are then presented. Section 3 contains a discussion of the stellar properties of the optical companion, Wray 977. Through a careful consideration of the parameters of the binary system, we have placed an upper limit on the mass and radius of the companion, which argues against the

[1] Current address: Department of Physics and Department of Astronomy, University of California, Berkeley, CA 94720.
[2] Current address: Center for Space Research, Massachusetts Institute of Technology, Cambridge, MA 02139.
[3] Universities Space Research Association.
[4] Current address: RIKEN Institute, Wako-shi, Saitama 351-01, Japan.

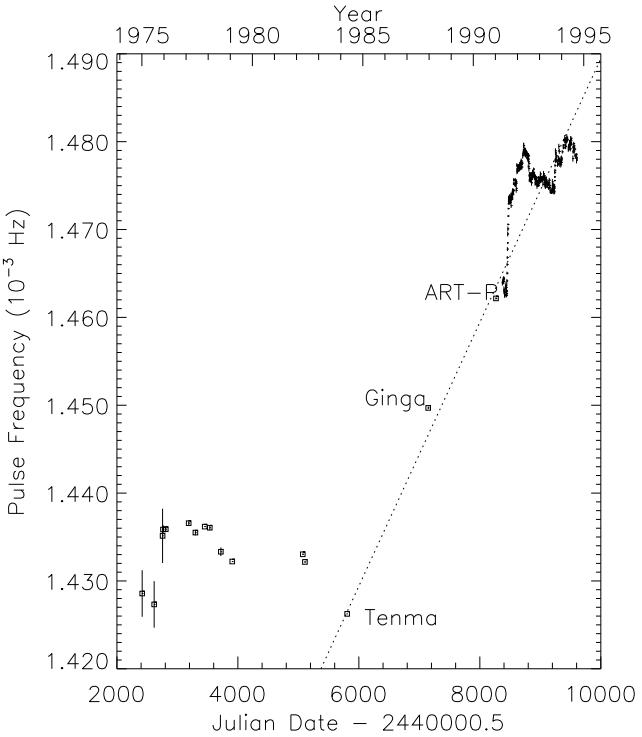


FIG. 1.—Pulse frequency history of GX 301−2 reduced to the solar system barycenter. The historical data are mostly taken from Nagase (1989). A 1991 measurement with ART-P/*Granat* (Lutovinov et al. 1994) and our 1991–1994 measurements with BATSE are also shown. The dotted line is the best linear fit to the *Tenma*, *Ginga*, and ART-P measurements that shows the spin-up trend that began in 1984. The gap near JD 2,448,700 is due to a tape recorder failure on *Compton*.

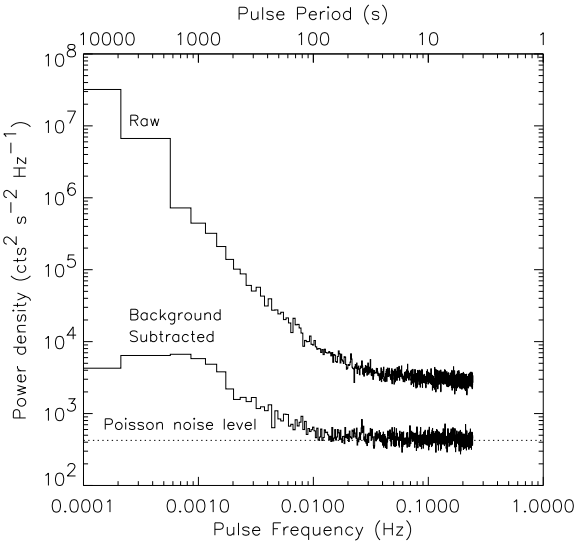


FIG. 2.—The typical power spectrum of the BATSE LAD background in the 25–33 keV range. The data shown are for CONT channel 1 (25–33 keV) from LAD 2 on MJD 48,851–48,852 when the mean count rate was 423.72 counts $s^{-1}$. The top curve is the unprocessed raw data, while the bottom curve is after background subtraction.

reclassification by Kaper et al. (1995, hereafter K95) of Wray 977 as a B1 Ia+ hypergiant. In § 4, we examine critically the possible mass transfer and accretion mechanisms at work in GX 301−2 and raise some theoretical issues that need to be addressed for this binary. Specifically, we show that most features of the folded flux profile can be understood if the neutron star were moving in the plane of a dense, slowly expanding circumstellar disk around Wray 977, whose existence was first postulated by Pravdo et al. (1995). We close in § 5 by arguing that the neutron star is primarily a wind-fed accretor, but that transient accretion disks can sometimes form that rapidly spin up the pulsar. We also summarize our results and suggest observations that may resolve some of the outstanding questions.

## 2. BATSE OBSERVATIONS AND FREQUENCY MEASUREMENTS

BATSE consists of eight identical uncollimated detectors positioned on the corners of the *Compton* spacecraft, providing an all-sky monitor of hard X-ray and $\gamma$-ray flux (Fishman et al. 1989). We used the CONT data (16 energy channels at 2.048 s resolution) from the BATSE large-area detectors (LADs), each of which has an effective area of $\approx 1000$ cm$^2$ from 30 to 200 keV. For frequency measurements, we used data in the approximate range 15–55 keV (channels 0–3). We only use channels 1–3 for flux measurements, since channel 0 is not well calibrated.

We begin by subtracting the mean background count rate (using the model of Rubin et al. 1996) from the raw data. The resultant reduction in the noise at low frequencies is displayed in Figure 2, where we show the power spectrum of the BATSE LAD background for CONT channel 1 (20–33 keV) before and after background subtraction. At frequencies $\nu \gtrsim 0.02$ Hz, the noise is consistent with Poisson counting statistics for the observed mean count rate of $C = 423.72$ counts $s^{-1}$. However, near the second (dominant) harmonic of GX 301−2 ($f = 0.003$ Hz), the noise level of the background-subtracted data is $\approx 7$ times the Poisson level. This translates into one-day and two-day 5 $\sigma$ detection threshold signal amplitudes of $\approx 0.8$ and 0.6 counts $s^{-1}$, respectively, for this channel. These thresholds agree with those obtained from simulations of injecting $\nu \approx 0.003$ Hz signals of varying amplitudes (1–20 counts $s^{-1}$) into the CONT channel 1 raw data. These signals were fully recovered, indicating that the background subtraction does not introduce any systematic effects.

In order to make a time series for the frequency searches, we summed the CONT channels 0–3 data weighted by the cosine squared[5] of the viewing angle for each detector and reduced all our timing observations to the solar system barycenter using the Jet Propulsion Laboratory DE-200 solar system ephemeris (Standish et al. 1992). The barycentric pulse frequency for each 1 day data segment was determined by searching the corresponding Fourier power spectrum for the strongest signal in a small range around the previously observed pulse frequency, always leading to detections near periastron ($\approx 5$ days before and after). The neutron star was only detected $\approx 50\%$ of the time outside this orbital phase interval. By increasing each observation interval to 2 days, we detected pulses away from periastron about 85% of the time.

[5] The angular response of the BATSE LADs deviates from the usual cos $\theta$ law below 100 keV because of the energy-dependent absorption by the metal and plastic shielding. Although the exact angular response depends on the intrinsic source spectrum, $\cos^2\theta$ is a good approximation over the range of power-law spectra typical for accreting pulsars (Chakrabarty 1996).

Pulse profiles were constructed by folding the time series of each (channel, detector) combination at the period determined from the Fourier power spectrum search. Profiles for which the second (dominant) harmonic is present at greater than 95% confidence are considered detections. We typically detected a pulse in CONT channels 1 (20–30 keV), 2 (30–45 keV), and 3 (45–55 keV) for two-day observations that detected the pulsar (at greater than 4 $\sigma$) in the summed (CONT channels 0–3) data. It was rare to see a pulse in channel 4, except near periastron passage. We never detected a pulse above channel 4, even in two-day observations. Figure 3 shows the pulse profiles as a function of channel for MJD 48,582–48,583 and MJD 48,632–48,633. No significant pulse shape changes are evident.

### 2.1. *Measuring the Neutron Star Orbit*

The neutron star orbit was first measured by S86 through a joint fit of pulse time-of-arrival (TOA) data from *Ariel 5*, *SAS 3*, and *Hakucho* observations. The orbital parameters they measured are shown in Table 1. The dashed line in Figure 4 displays the orbit-induced frequency derivative, $\dot{\nu}_{\rm orb}$, as a function of time for two orbits from S86's parameters. Due to the large eccentricity of the system, $\dot{\nu}_{\rm orb}$ changes abruptly over $\approx$4 days in the vicinity of the perias-

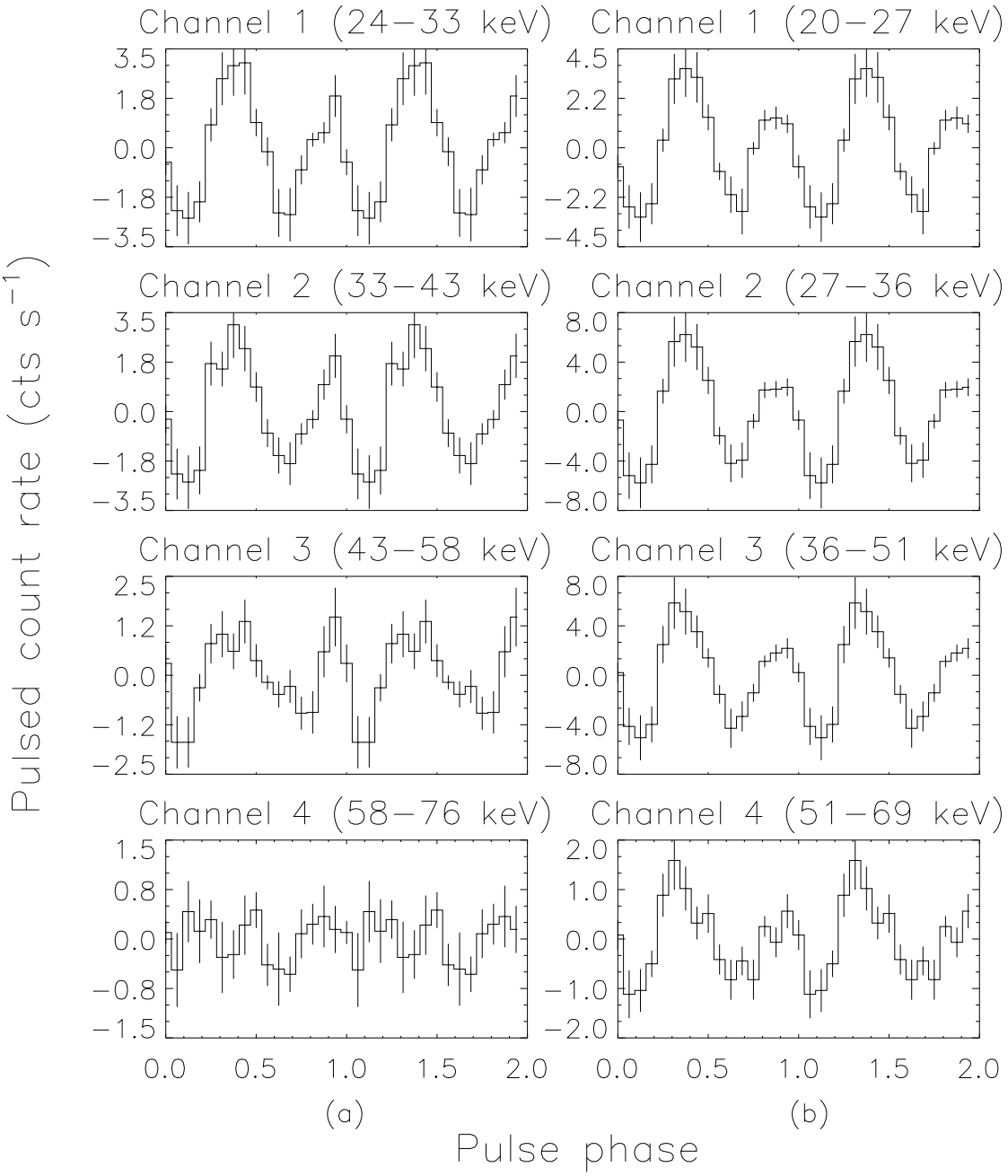


FIG. 3.—Pulse profiles as a function of energy for GX 301−2 during the interval (*a*) MJD 48,622–48,623 (orbital phase 0.68) and (*b*) MJD 48,632–48,633 (orbital phase 0.92). Two pulses are shown for each channel, and all channels are displayed relative to the same pulse phase. The energy edges for each CONT channel of BATSE detector 0 in (*a*) and 7 in (*b*) are indicated. The pulse shapes are uncorrected for the rapid change in detector response as a function of energy in the 20–75 keV range. While the double-peaked profile characteristic of this pulsar is clearly visible in channels 1–3, the pulse is only detected in channel 4 on MJD 48,632–48,633.

TABLE 1

GX 301−2 Orbital Parameters

| Parameter | Sato[a] | BATSE[a] | (BATSE + Sato)[a,b] |
|---|---|---|---|
| $P_{orb}$ (days)..... | 41.508 ± 0.007 | 41.488 ± 0.009 | 41.498 ± 0.002 |
| $a_x \sin i$ (lt-s)..... | 371.2 ± 3.3 | 370.0 ± 4.0 | 368.3 ± 3.7 |
| $e$..... | 0.472 ± 0.011 | 0.462 ± 0.014 | 0.462 ± 0.014 |
| $\omega$ (deg) ..... | 309.9 ± 2.6 | 311.3 ± 1.5 | 310.4 ± 1.4 |
| $T_0$[c] (MJD)..... | 43,906.06 ± 0.16 | 48,802.85 ± 0.13 | 48,802.79 ± 0.12 |

[a] Quoted uncertainties are single-parameter 1 $\sigma$ confidence limits.

[b] The $P_{orb}$ in this column was obtained by comparing the $T_0$ in the first two columns and assuming that $P_{orb}$ remained constant over this interval. The other four orbital parameters in this column were obtained by performing a least-squares fit with $P_{orb}$ fixed.

[c] Time of periastron passage.

tron passage. The 1 $\sigma$ error in the extrapolation of the time of periastron passage from S86 to the present date is $\approx 1$ day, clearly inadequate for correcting the observed frequencies to the pulsar rest frame. Hence, even if all other orbital parameters have remained constant since S86's data, it is essential to redetermine the best-fit time of periastron. We now describe our new measurement of this parameter, which gives the solid line in Figure 4.

A pulse profile template was constructed by accumulating 235 two-day profiles of channel 1 data from the detector with the best view of GX 301−2 for MJD 48,370–49,354. Rather than use the traditional cross-correlation technique to find the shift between a pulse profile and a template, we employed a cross-spectrum technique (Bendat & Piersol 1986; see Appendix A). In addition to computing the phase shift more accurately, this technique defines the statistical contributions to TOA errors. Both techniques assume that the pulse shape noise is white (Appendix A and Deeter & Boynton 1986), whereas the background at low frequencies (Rubin et al. 1996) reddens the pulse shape noise. To alleviate this, we filtered the pulse profiles in the frequency domain by attenuating their harmonic components by the ratio of the expected white noise power to the measured noise power at the harmonic frequency (Deeter & Boynton 1986). In the vicinity of periastron passage, $0.85 \lesssim \phi_{orb} \lesssim 1.1$, GX 301−2 was usually bright enough to measure a TOA once per day. At other orbital phases, accurate TOAs could only be obtained at two-day intervals.

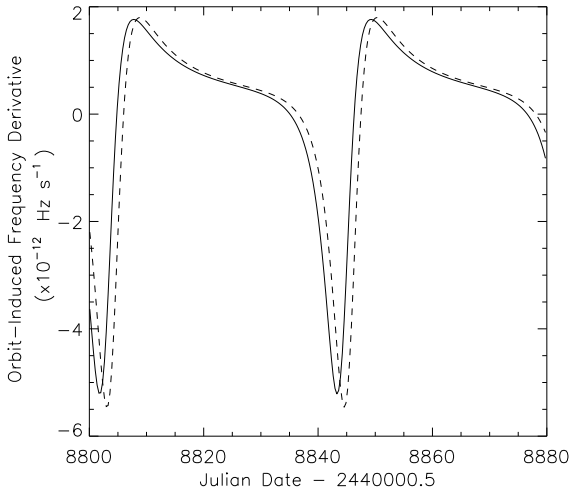


Fig. 4.—The orbit-induced frequency derivative of the pulsar, $\dot{\nu}_{orb}$, as a function of time for two orbits. The solid line is from our orbital parameters, while the dashed line is from the orbital parameters of S86.

Measuring the neutron star orbit is complicated by the need to decouple the orbital Doppler delays from any intrinsic changes in the neutron star rotation rate. This is especially true near periastron, where orbital accelerations are large and the torques on the neutron star might also increase. Variations in the intrinsic pulse period prohibited us from maintaining an accurate pulse count over more than one orbit, so we employed a "hybrid" approach to determining the orbit. We write the pulse emission times as

$$t'_n = t'_0 + \frac{n}{\nu_0} - n^2 \frac{\dot{\nu}}{2\nu_0^3}, \quad (1)$$

where $t'_0$ is the emission time epoch, and $\nu_0$ and $\dot{\nu}$ are the pulse frequency and its derivative at $t'_0$. The arrival times are then $t_n = t'_n + g(t'_n)$, where $g(t'_n)$, the orbital time delay, is parametrized by five Keplerian orbital parameters: the projected semimajor axis $a_x \sin i$ (where $i$ is the inclination angle between the line of sight and the orbital angular momentum vector, defined to lie in the first quadrant), the orbital period $P_{orb}$, the eccentricity $e$, the longitude of periastron $\omega$, and the orbital epoch $T_0$ (defined as the epoch of periastron passage).

The five orbital parameters, along with independent $t'_0$, $\nu_0$, and $\dot{\nu}$ for each orbit, were estimated simultaneously by a least-squares fit of the TOAs. To minimize any bias introduced by possibly large $|\dot{\nu}|$ values at periastron, we typically begin timing in the vicinity of apastron (orbital phase = 0.5) and only used data from orbits for which a pulse could be detected over most ($\gtrsim 80\%$) of the orbit. Sudden torque fluctuations and low fluxes rendered $\approx 50\%$ of the orbits unusable for TOA analysis.

We varied all five orbital parameters in our fitting, starting with S86's parameters as the initial guess. By comparing our best-fit $T_0$ with that of S86, and assuming that $P_{orb}$ has remained constant over this interval, we obtained a refined value of $P_{orb} = 41.498 \pm 0.002$ days. We then fix $P_{orb}$ at this value and allow the other four orbital parameters to vary. These orbital parameters, together with those determined by S86 and those determined from the BATSE data only, are shown in Table 1. There are no statistically significant differences in the orbital solutions, and thus no evidence for apsidal motion or orbital decay at present. Figure 5 shows the best-fit delay curve with our model of $\nu_0$ and $\dot{\nu}$ removed from each timing interval. The statistical errors in the TOAs computed by the cross-spectrum technique are $\approx 3$–6 s, much smaller than the rms arrival time fit residuals of $\approx 20$ s. Since we do not know the origin of this discrepancy, we assigned a constant error of 20 s to all TOAs when performing the orbital fit.

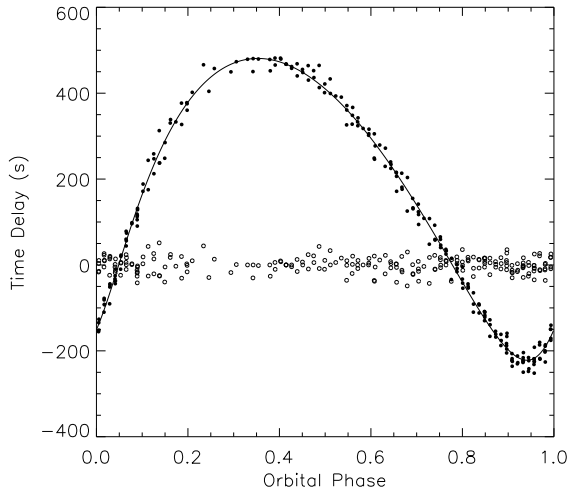


FIG. 5.—Time delays for the pulse arrival times as a function of the orbital phase of GX 301−2 after removing our best model for the intrinsic variations in the spin period. The data plotted are from the interval MJD 48,370–49,354. The filled circles are the delay times, the solid curve is the best-fit orbital model, and the open circles are the residuals.

### 2.2. *The Neutron Star Spin Frequency History*

The neutron star spin frequency history from MJD 48,370–49,612 is shown in Figure 6. The star generally experiences fluctuating accretion torques with $\langle |\dot{\nu}| \rangle \approx 2.5 \times 10^{-14}$–$2.2 \times 10^{-13}$ s$^{-2}$. Approximately on yearly timescales, the star alternates between mild spin-up and spin-down, with $\langle |\dot{\nu}| \rangle \approx 2.0 \times 10^{-13}$ s$^{-2}$. However, there are also two dramatic spin-up episodes (MJD 48,440–48,463 and MJD 49,230–49,245), which we discuss below. In order to search for systematic torque variations with orbital phase, we folded the frequency derivative measurements at $P_{\rm orb}$. These frequency derivatives were computed by taking time derivatives of two-day frequency measurements, excluding the two major spin-up episodes. There is no strong evidence for spin-up or spin-down torques at any particular orbital phase.

### 2.3. *Hard X-Ray Spectrum and Flux Measurements*

The pulse is detected in CONT channels 1–4 (20–75 keV) in the vicinity ($\pm 5$ days) of periastron passage. Outside of periastron, it is only detected in channels 1–3 (20–55 keV). We extended the pulse detections to channel 5 by combining data for many days. We first folded all channels of the CONT data (only from the detector with the smallest viewing angle to the source) at one-day intervals at the known pulse frequencies, as determined from our fast Fourier transform search. A coherent pulse profile was built up from these 1 day profiles by measuring the phase shift between each daily profile and the running sum with a cross-correlation analysis, by phase shifting the profiles, and by adding to the running sum those profiles of high signal-to-noise ratio. For each profile included into the running sum, a running sum of the corresponding detector response matrices was also kept.

We generated four different spectra, which spanned a range of luminosities and orbital phases, with data near periastron, near apastron, away from periastron and apastron, and from the spin-up episodes. The count rate energy distributions were fitted by a power-law photon spectrum of the form $(dN/dE)_{\rm pl} \propto (E/30\ {\rm keV})^{-\gamma}$ and an optically thin thermal bremsstrahlung (OTTB) spectrum of the form $(dN/dE)_{\rm OTTB} \propto (1/E) \exp(-E/kT) g_{\rm ff}(E, kT)$, where $g_{\rm ff}$ is the velocity-averaged Gaunt factor. The coverage of the different spectra and their corresponding best-fit spectral parameters are shown in Table 2.

Figure 7 shows the spectral fits to the near periastron data for both models. The reduced $\chi^2$ for the OTTB fit is 1574, while that for the power-law fit is 2369. Although the OTTB is a better representation of the spectrum, the 25–100 keV pulsed fluxes inferred from the power-law and OTTB fits are almost identical at, respectively, 1.175 and $1.197 \times 10^{-9}$ ergs cm$^{-2}$ s$^{-1}$. We could not detect any appreciable changes in spectral shapes, so that flux differences are largely reflected by changes in $C_{30}$, which is $dN/dE$ evaluated at $E = 30$ keV. Since the power law yields a good measure of the flux in the bandpass, we fixed $\gamma$ at 4.5 and measured the pulsed flux every 2 days. Only pulse profiles from channels 1–3 (20–55 keV) were used, since we do not always detect the pulse in channel 4 (55–75 keV). The count rate in a pulse profile was obtained by assuming that each profile is a shifted, scaled version of the template. The method used to find the amplitude scaling, $I$, is detailed in Appendix B. Only data from the detector with the best viewing angle to the source were used. For all two-day data segments that registered detections in at least channels 1 and 2, $C_{30}$ was computed (for $\gamma = 4.5$). Figure 8 shows the 20–55 keV pulsed flux as a function of time for MJD 48,370–49,612. This plot shows that the flux is always high at periastron and drops off dramatically outside of periastron.

Figure 9 displays these flux measurements folded at the orbital period, excluding the two spin-up episodes that we will discuss separately. Consistent with earlier observations (S86; Chichkov et al. 1995; Pravdo et al. 1995), we find that the pulsed flux peaks slightly before periastron, at orbital phase $0.956 \pm 0.022$. A smaller flare occurs near apastron at

TABLE 2

GX 301−2 SPECTRAL PARAMETERS

| Coverage | Power Law[a] ($\gamma$, $C_{30}$) | OTTB[a,b] ($kT$, $C_{30}$) |
|---|---|---|
| Periastron ($0.80 < \phi_{\rm orb} < 1.10$) | $4.675 \pm 0.010$, $1.450 \pm 0.003$ | $14.40 \pm 0.06$, $2.25 \pm 0.07$ |
| Apastron ($0.35 < \phi_{\rm orb} < 0.65$) | $4.527 \pm 0.019$, $0.816 \pm 0.004$ | $13.58 \pm 0.10$, $1.36 \pm 0.07$ |
| Others ($0.10 < \phi_{\rm orb} < 0.35$ and $0.65 < \phi_{\rm orb} < 0.80$) | $4.338 \pm 0.020$, $0.580 \pm 0.003$ | $14.47 \pm 0.12$, $0.93 \pm 0.06$ |
| Spin-up episodes (MJD 48,450–48,470 and MJD 49,231–49,250) | $4.761 \pm 0.033$, $1.387 \pm 0.009$ | $14.00 \pm 0.17$, $2.20 \pm 0.20$ |

[a] $C_{30}$ is $dN/dE$ evaluated at $E = 30$ keV and has units of $10^{-3}$ cm$^{-2}$ s$^{-1}$ keV$^{-1}$.
[b] $kT$ in units of keV.

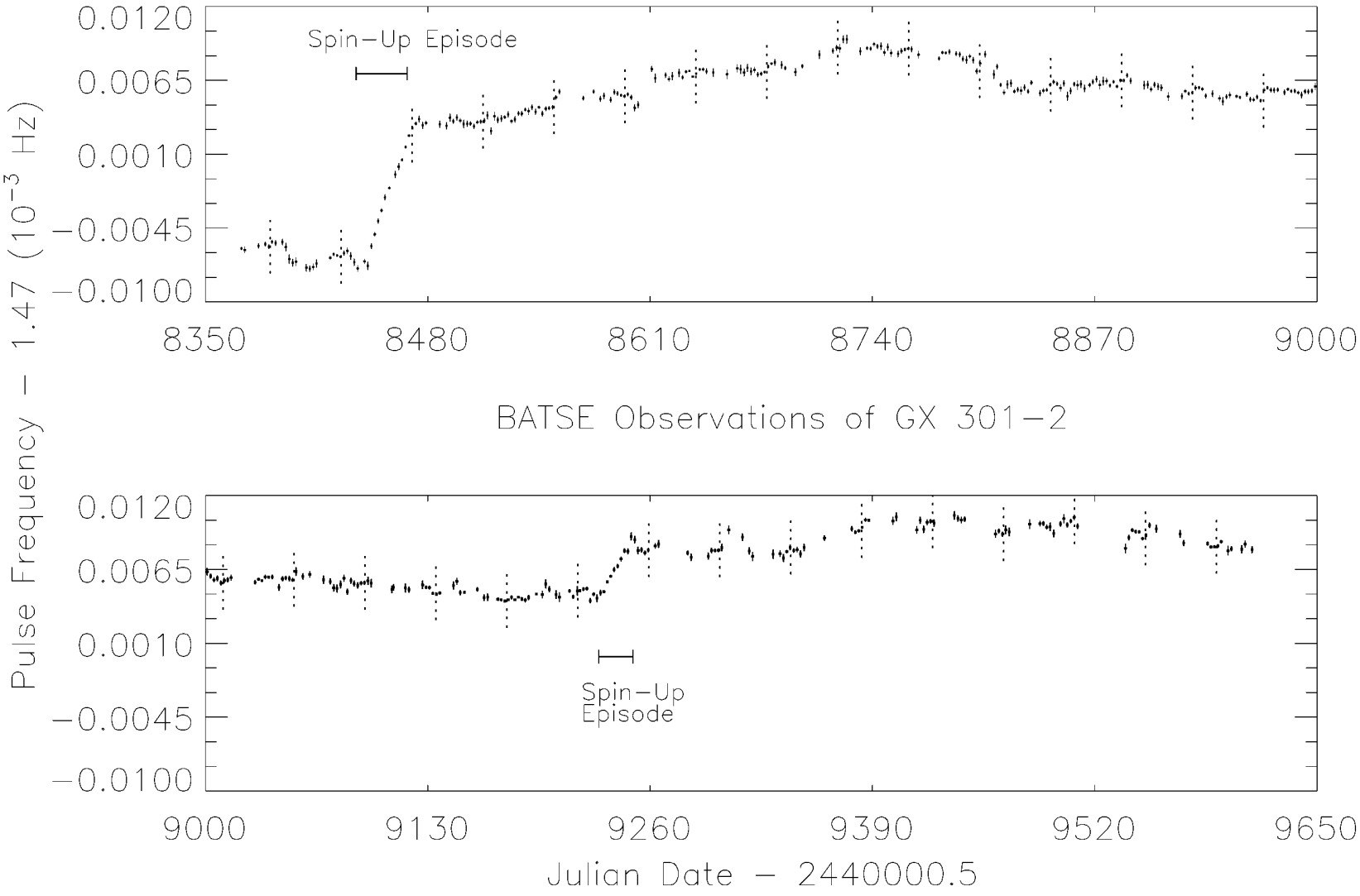


FIG. 6.—The intrinsic neutron star spin frequency in GX 301−2 from MJD 48,370–49,612. The dotted lines indicate periastron passages. We also mark the two rapid spin-up episodes.

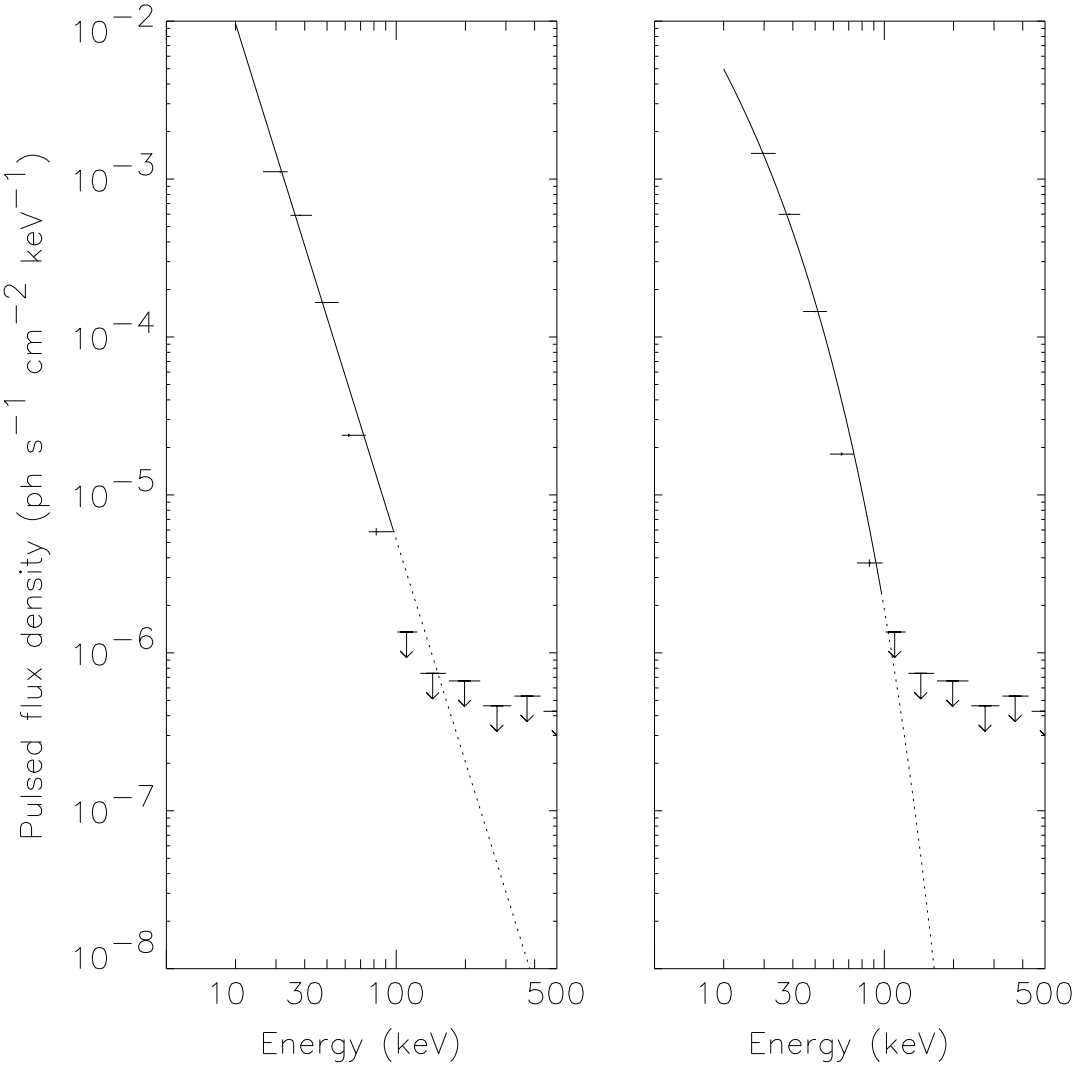


FIG. 7.—The phase and time-averaged pulsed photon spectrum of GX 301−2 for all days in the vicinity of periastron passages ($0.80 < \phi_{orb} < 1.10$). *Left panel*: the solid line represents the best fit to the spectral model $dN/dE = C_{30}(E/30\ \mathrm{keV})^{-\gamma}$, for which $\gamma = 4.675 \pm 0.010$ and $C_{30} = (1.4498 \pm 0.0030) \times 10^{-3}$ cm$^{-2}$ s$^{-1}$ keV$^{-1}$. *Right panel*: the solid line is the best-fit OTTB model with $kT = 14.40 \pm 0.06$ keV and a value at 30 keV of $(2.25 \pm 0.06) \times 10^{-3}$ cm$^{-2}$ s$^{-1}$ keV$^{-1}$ for the same data set, which is a better fit according to $\chi^2$.

orbital phase $0.498 \pm 0.057$ and was also found by Pravdo et al. (1995) and Chichkov et al. (1995). The typical periastron flare is a change in the 20–55 keV flux from $1.0 \times 10^{-9}$ to $2.7 \times 10^{-9}$ ergs cm$^{-2}$ s$^{-1}$. For a typical apastron flare, the 20–55 keV flux increases from $1.0 \times 10^{-9}$ to $1.4 \times 10^{-9}$ ergs cm$^{-2}$ s$^{-1}$. The flux is high enough near periastron to be measured by the Earth occultation technique (Harmon et al. 1992). The few simultaneous measurements show that the pulsed 20–55 keV flux is about one-half of the (unpulsed + pulsed) component. Multiple observations by WATCH/*Granat* from MJD 47,900–49,300 yield an average 1–20 keV flux at periastron of $\approx 3.6 \times 10^{-8}$ ergs cm$^{-2}$ s$^{-1}$ (Chichkov et al. 1995). Thus, only $\approx 8\%$ of the total flux is detected as pulsed emission in the BATSE bandpass.

## 3. INFERENCES ABOUT THE OPTICAL COMPANION

There have been many observations of the massive stellar companion of GX 301−2. Here we first constrain the mass and radius of the companion and then discuss the properties of its stellar wind.

### 3.1. *Constraints on the Mass and Radius of the Optical Companion*

We now combine our orbital measurements with K95's measurements to constrain the mass and radius of the optical companion. Wray 977 is a supergiant with $V = 10.83$ (Hammerschlag-Hensberge, Zuiderwijk, & van den Heuvel 1976), $B-V = 1.76$ (Bord et al. 1976). K95's spectral classification (B1 Ia+) implies $T_{\rm eff} \approx 20{,}000$ K, an intrinsic color index of $(B-V)_0 = -0.20$ (Bohm-Vitense 1981), and a bolometric correction for the $V$ band $BC_V = -1.87$ (Schmidt-Kaler 1982). The bolometric flux, corrected for reddening ($A_V = 5.88$), is then $F_{\rm bol} \approx 1.45 \times 10^{-6}$ ergs cm$^{-2}$ s$^{-1}$. The resulting relationship between the companion radius, $R_c$, and the distance to the binary, $D$, is

$$R_c \approx 17.7\ R_\odot \left(\frac{D}{1\ \mathrm{kpc}}\right)\left(\frac{20{,}000\ \mathrm{K}}{T_{\rm eff}}\right)^2 . \quad (2)$$

The orbital period and projected semimajor axis of the neutron star orbit yield a mass function

$$f(M_x) = \frac{(M_c \sin i)^3}{(M_x + M_c)^2} = 31.8\ M_\odot , \quad (3)$$

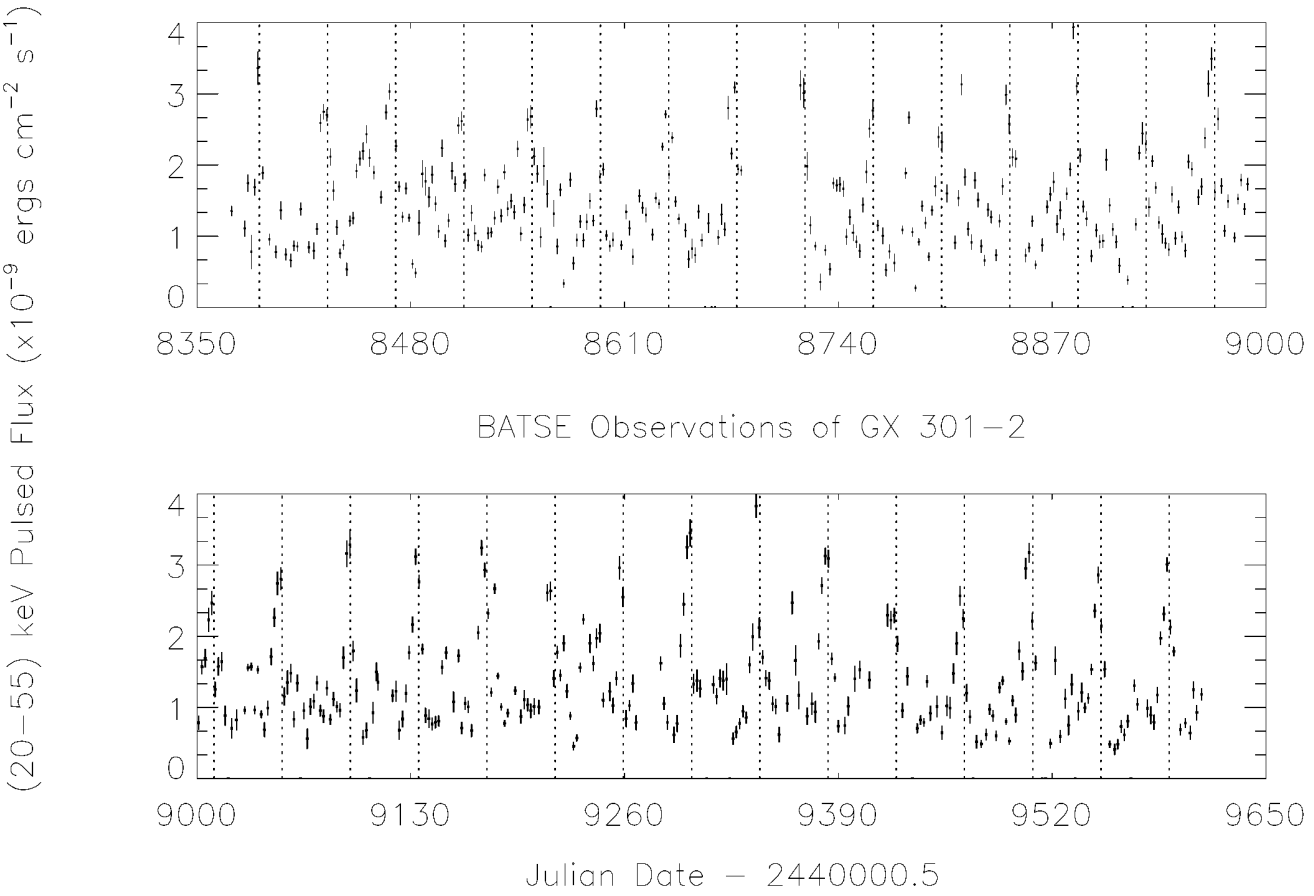


FIG. 8.—The 20–55 keV pulsed flux from MJD 48,388–49,612. These fluxes were found for a presumed photon number index of 4.5, using only the detector with the smallest viewing angle to the source.

which requires the companion mass, $M_c$, to be $\geq 35\ M_\odot$ for a neutron star mass of $M_x = 1.4\ M_\odot$.

A star this massive can only reach the effective temperature of a B-type star through nuclear evolution for $\geq 10^6$ yr. For the purposes of constraining the companion mass, we derived an $L(M)$ relation from the Schaller, Schaerer, & Maeder (1992) models of massive (between 24 and 81 $M_\odot$) evolved stars with $T_{\rm eff} \approx 20{,}000$ K for both high and low metallicity. The resulting relationship

$$L \approx 3 \times 10^5\ L_\odot \left(\frac{M}{30\ M_\odot}\right)^{1.8} \quad (4)$$

scales with mass as one would obtain from the Eddington standard model (Hansen & Kawaler 1994) (for a mean molecular weight $\mu = 0.6$) when, as appropriate for this mass range, radiation pressure is becoming appreciable. This $L(M)$ relation is slightly brighter than that for zero-age main sequence because of the helium enrichment of the core. The Thomson scattering appropriate for these stars implies that they radiate at a rate nearly independent of their radius, so that we can use this $L(M)$ for the full range of masses in the interpolated range.

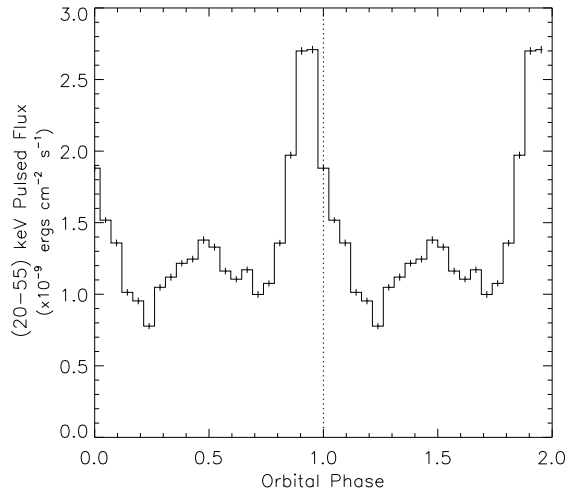


FIG. 9.—The 20–55 keV pulsed flux from MJD 48,388–49,612 as a function of orbital phase. Fluxes from the spin-up episodes (MJD 48,440–48,463 and MJD 49,230–49,245) have been excluded. The periastron flare peaks at orbital phase $0.956 \pm 0.022$. Another significant peak occurs at orbital phase $\approx 0.5$. Orbital phases 0 and 1 are periastron passages.

The hatched region in Figure 10 denotes the companion radius as a function of mass using the $L(M)$ relation in equation (4) and taking 20,000 K $< T_{\rm eff} <$ 22,000 K. We have chosen a range of effective temperatures to reflect some of the uncertainty in spectral type. The radius of the star must lie below the dark solid line, since no eclipse is observed, so that $M_c > 39\ M_\odot$. The star must also be smaller than the physical separation at periastron (denoted by the light solid line), placing an upper limit of $M_c <$ 80–100 $M_\odot$ that depends on $T_{\rm eff}$.

A more stringent mass constraint comes from considering the tidal distortion of the companion during periastron passage. The $l = 2$ $f$-mode will establish an equilibrium tide when its natural frequency, $\omega_f$, is much larger than the characteristic perturbing frequency at periastron passage, $\Omega_p = (1 - e^2)^{1/2} 2\pi/[P_{\rm orb}(1 - e)^2]$ (Kumar, Ao, &

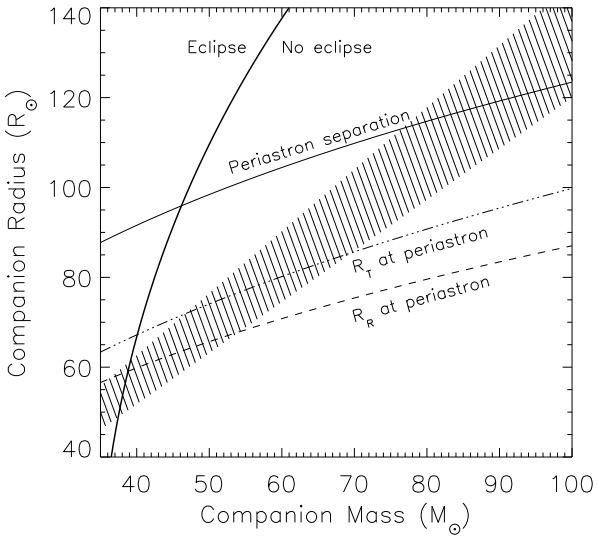


FIG. 10.—Mass-radius constraints to the optical companion Wray 977. The upper heavy solid line is the condition for an eclipse. The $R(M)$ relation for the companion is shown by the hatched region, where we allow for some uncertainty in $T_{\rm eff}$. The lower solid line is the separation between the neutron star and the stellar companion at periastron. The Roche (tidal) lobe radius at periastron is denoted by the dashed (dot-dashed) line.

Quataert 1995). The massive star is well represented by an $n = 3$ polytrope, which is very centrally condensed and has $\omega_f^2 = 8.2GM_c/R_c^3$ for $l = 2$ (Cox 1980). Using the $L(M)$ relation above, we find that $P_f \approx 3$ days $(20{,}000/T_{\rm eff})^3(M/40\ M_\odot)^{0.85}$, so that $\omega_f/\Omega_p \approx 4.5$. The dynamical tide also excites a resonant response (which would not be in instantaneous equilibrium), but the amplitude scales as $\exp(-\alpha_e\omega_f/\Omega_p) \sim 10^{-3}$ with $\alpha_e \approx 1.3e^{-0.25}$ ($e$ is the orbital eccentricity). Thus, the companion star essentially responds adiabatically even at periastron, and we can safely assume that it is instantaneously in tidal equilibrium. We thus use the fitting formulae of Joss & Rappaport (1984) for estimating both the Roche (corotating) lobe and the tidal (no rotation) lobe of the star at periastron. We view the tidal lobe as a limiting case since the measured rotational velocity, $v \sin i_r \approx 70$ km s$^{-1}$ (Parkes et al. 1980), is much less than that needed for corotation at the periastron period.

The Roche and tidal radii are plotted in Figure 10. If we require that the star not overflow its tidal lobe at periastron, then $M_c < 70\ M_\odot$, $R_c < 85\ R_\odot$, and $D < 5.8$ kpc for $T_{\rm eff} = 22{,}000$ K, while $M_c < 47\ M_\odot$, $R_c < 72\ R_\odot$, and $D < 4.1$ kpc for $T_{\rm eff} = 20{,}000$ K. If the star does not overflow the Roche lobe at periastron, then $M_c < 55\ M_\odot$, $R_c < 68\ R_\odot$, and $D < 4.3$ kpc for $T_{\rm eff} = 22{,}000$ K. These are all consistent with $D \approx 1.8$ kpc inferred by Parkes et al. (1980). We are nearly in conflict with K95's conclusions that the binary is at $D = 5.3$ kpc and has $L = 1.3 \times 10^6\ L_\odot$. This requires a $68\ M_\odot$ star with a radius so large as to only be marginally consistent with the tidal constraint for an unusually high effective temperature of $T_{\rm eff} \gtrsim 21{,}100$ K. Masses this large have rarely been measured dynamically. One of the most massive Wolf-Rayet stars with a dynamical mass limit is WR 22 (HD 92740), with $M > 72\ M_\odot$ (Rauw et al. 1996). Further optical and near-UV observations of Wray 977 are needed to better constrain $T_{\rm eff}$ and $L$.

There are three other known pulsars accreting from the winds of supergiant companions: Vela X-1, 4U 1538−52, and 4U 1907+09. The companion mass for GX 301−2 is more than twice that of Vela X-1 and 4U 1538−52, for which $M_c \approx 20\ M_\odot$ (Nagase 1989). In contrast to the high eccentricity of GX 301−2, the orbits of Vela X-1 and 4U 1538−52 are nearly circular, potentially because of more rapid circularization in the tighter orbit and the larger age of these systems.

### 3.2. *The Stellar Wind*

The optical spectrum has P Cygni line profiles in the hydrogen Balmer (up to H$\gamma$) and Helium emission lines, thus indicating a strong stellar wind (Parkes et al. 1980; K95). The interstellar extinction prohibits measuring the terminal wind velocity from UV resonance lines, in which case K95 assumed that $v_\infty = 400$ km s$^{-1}$ and found that $\dot{M}_W \lesssim 10^{-5}\ M_\odot$ yr$^{-1}$. The H$\alpha$ equivalent width measured by K95 is 7.1 Å, which is larger than that of 5.2 for $\eta^1$ Sco, a well-known B hypergiant. This led K95 to suggest that Wray 977 was exceedingly luminous. This might very well be the case and, if true, only exacerbates the difficulties discussed above with overfilling the tidal lobe at periastron.

## 4. MASS TRANSFER AND ACCRETION ONTO THE NEUTRON STAR

GX 301−2 can accrete from the stellar wind of its companion, but the two rapid and long-lasting spin-up episodes are unusual for stellar wind accretion. Comparable events have not been seen in other persistent high-mass X-ray binaries accreting via winds. In contrast, matter transferred from an accretion disk to the neutron star has a definite sense of angular momentum and can give rise to a monotonic increase in the neutron star spin frequency.

### 4.1. *The Two Rapid Spin-Up Episodes*

Figure 11 shows $\nu$, $\dot{\nu}$, and the pulsed hard X-ray flux for the two rapid spin-up episodes: MJD 48,440–48,463 (*left panels*) and MJD 49,230–49,245 (*right panels*). The measured $\dot{\nu}$ values between MJD 48,443–48,463 and MJD 49,231–49,245 are $\dot{\nu} \approx 4.5 \times 10^{-12}$ Hz s$^{-1}$ and $\dot{\nu} \approx 3.0 \times 10^{-12}$ Hz s$^{-1}$, respectively, giving a spin-up timescale $\approx \nu/\langle\dot{\nu}\rangle \approx 10$ yr. The steady spin-up strongly suggests that the neutron star is accreting from an accretion disk during these intervals. The fluxes are also higher than usual for these orbital phases. The 20–55 keV flux averaged over MJD 48,443–48,458 (orbital phase 0.35–0.70) is $(1.889 \pm 0.037) \times 10^{-9}$ ergs cm$^{-2}$ s$^{-1}$, whereas the folded flux history averaged over the same orbital phase yields $(1.216 \pm 0.008) \times 10^{-9}$ ergs cm$^{-2}$ s$^{-1}$. For the second spin-up episode, the 20–55 keV flux averaged over MJD 49,233–49,245 (orbital phase 0.37–0.66) is $(1.926 \pm 0.042) \times 10^{-9}$ ergs cm$^{-2}$ s$^{-1}$ compared with the folded flux history value for the same orbital phase of $(1.239 \pm 0.010) \times 10^{-9}$ ergs cm$^{-2}$ s$^{-1}$.

The magnetospheric radius must be less than the corotation radius $r_{\rm co} = 1.3 \times 10^{10}$ cm (where a Keplerian disk corotates with the neutron star) in order for the material to flow freely along the magnetic field lines and onto the neutron star. The maximum specific angular momentum transferred to the neutron star is then $l_{\rm max} \equiv (GM_x r_{\rm co})^{1/2}$. This allows us to set a lower limit on $\dot{M}$ given $\dot{\nu}$, as $N_{\rm obs} = 2\pi I\dot{\nu} < \dot{M} l_{\rm max}$ (Chakrabarty et al. 1993). We then find for $M_x = 1.4\ M_\odot$,

$$\dot{M} > 2 \times 10^{-10}\ M_\odot\ {\rm yr}^{-1}\left(\frac{\dot{\nu}}{3 \times 10^{-12}\ {\rm s}^{-2}}\right)\left(\frac{R}{10\ {\rm km}}\right)^2, \quad (5)$$

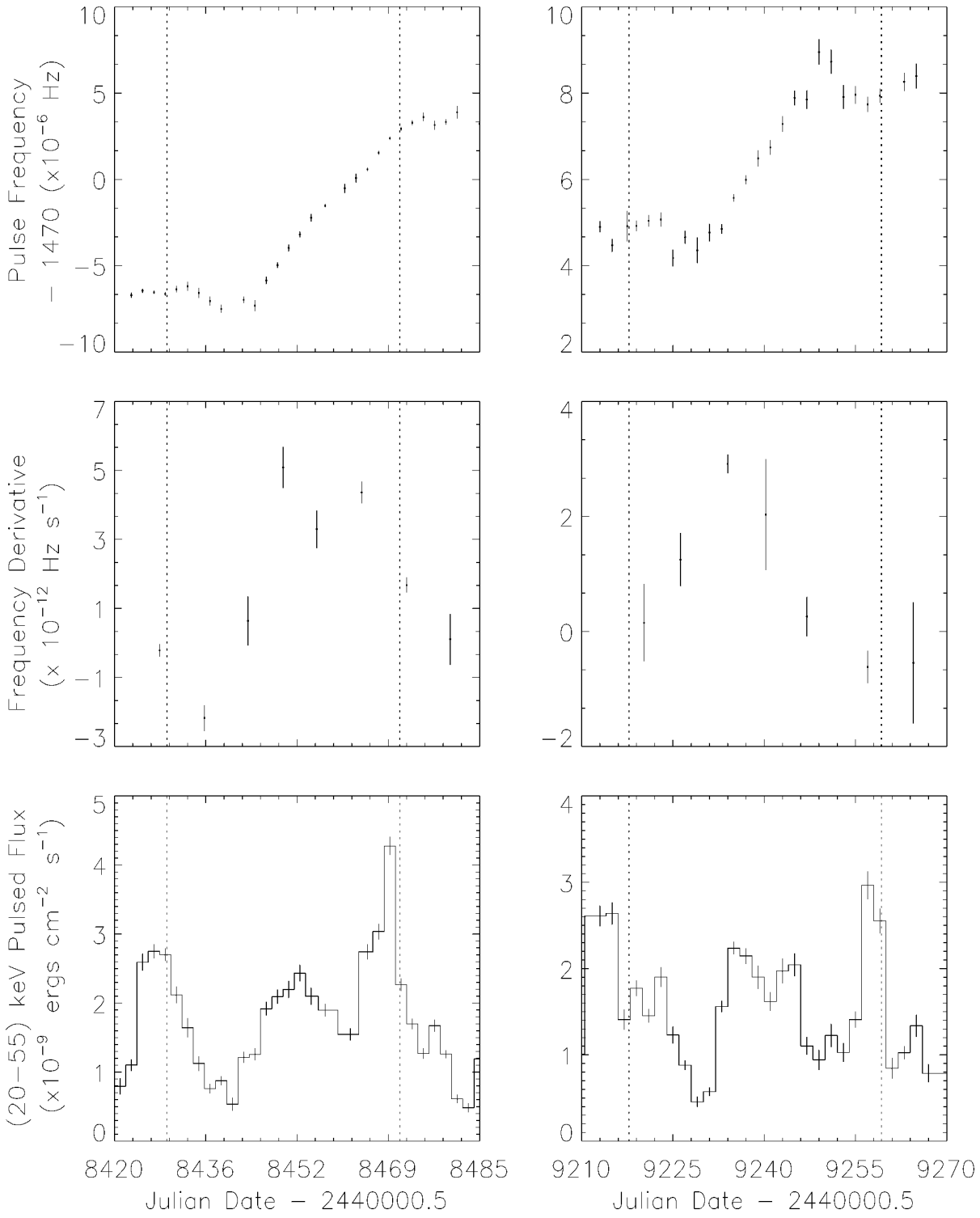


FIG. 11.—Frequency, frequency derivative, and pulsed flux during the spin-up episodes that occurred on MJD 48,440–48,463 (*left panels*) and MJD 49,230–49,245 (*right panels*). The vertical dotted lines denote periastron passage. The onset of spin-up is accompanied by an increase in the 20–55 keV flux. The 20–55 keV flux averaged over MJD 48,443–48,458 (orbital phase 0.35–0.70) is $(1.889 \pm 0.037) \times 10^{-9}$ ergs cm$^{-2}$ s$^{-1}$, while for MJD 49,233–49,245 (orbital phase 0.37–0.66) it is $(1.926 \pm 0.042) \times 10^{-9}$ ergs cm$^{-2}$ s$^{-1}$.

where $I = 0.4 M_x R^2$ is the neutron star moment of inertia (Ravenhall & Pethick 1994). The measured $\dot{\nu}$ values of $4.5 \times 10^{-12}$ and $3.0 \times 10^{-12}$ Hz s$^{-1}$ imply $L_x > 3 \times 10^{36}$ ergs s$^{-1}$, in agreement with the 1–20 keV WATCH/*Granat* luminosity measurements (Chichkov et al. 1995) of $\approx 10^{37}$ ergs s$^{-1}$ at periastron for a distance of 1.8 kpc. Of course, the magnetosphere could be closer to the star than the corotation radius.

Both spin-up events begin just after periastron. The infrequent occurrence of these episodes argues against the hypothesis that the event is triggered by tidal overflow at periastron. However, especially if the companion is as lumi-

nous as K95 infer, the episodes might be accretion of matter ejected in a mass-loss episode from the star, similar to what is seen from luminous blue variables (LBVs). The luminosity, mass, and $T_{\rm eff}$ of Wray 977 put it squarely in the regime where LBVs undergo large-scale mass-loss episodes every 2–10 yr (Stothers & Chin 1995). It may be that the expelled matter is captured predominantly at periastron, in which case the delay between the periastron passage and the onset of the torque is the viscous timescale in the accretion disk. The total mass accreted by the neutron star during a spin-up episode is greater than $2 \times 10^{-11}\ M_\odot$, comparable to the mass in an $\alpha = 0.1$ disk of outer radius $R \sim 10^{10}$ cm, for which the viscous time is about 10–30 days, the same as the duration of the spin-up event.

### 4.2. *Accretion from the Companion's Wind*

Excluding the spin-up episodes, the neutron star experiences torques of both signs, independent of orbital phase, resulting in nearly no frequency change over our observation interval. This is consistent with two-dimensional simulations of wind accretion by Fryxell & Taam (1988) and Taam & Fryxell (1989). They showed that accretion from a stellar wind is highly time-dependent; transient accretion disks form and persist for a few flow times across the accretion diameter (approximately hours for GX 301−2) before dissipating, only to be replaced by disks rotating in the opposite direction. This flip-flop behavior results in large specific angular momentum transfer on short timescales but little net angular momentum change on long timescales.

This behavior motivates the simplest model of supersonic Bondi-Hoyle accretion from the spherical wind of the companion, which predicts the neutron star accretion rate, $\dot{M}$, to be

$$\dot{M} = \frac{\dot{M}_W G^2 M_x^2 \delta^3}{a^2 v_W^4(a)}\,, \tag{6}$$

where $a$ is the distance between the companion and the neutron star, $v_W$ is the wind velocity at the neutron star, and $\delta = v_W/v_{\rm rel}$ ($v_{\rm rel}$ is the relative velocity between the neutron star and the wind). Following Castor, Abbott, & Klein (1975), we write

$$v_W(r) = v_\infty\left(1 - \frac{R_c}{r}\right)^\beta\,, \tag{7}$$

where $v_\infty$ is the terminal velocity of the wind and $\beta = 0.5$. A refined treatment by Friend & Abbott (1986) yields $\beta = 0.8$, the value that we adopt. However, the spherical wind model does not predict the observed secondary flux peak at $\phi_{\rm orb} \approx 0.5$. Moreover, for $\dot{M}_W = 3 \times 10^{-6}\ M_\odot\ {\rm yr}^{-1}$ and $v_\infty \approx 1000$ km s$^{-1}$ (Parkes et al. 1980), we get $\dot{M} \approx 4 \times 10^{-10}\ M_\odot\ {\rm yr}^{-1}$ at periastron and a ratio of the maximum to minimum flux of $\approx 50$. If we adopt $v_\infty = 400$ km s$^{-1}$ (K95), then the maximum-to-minimum flux ratio drops to $\approx 12$. Both of these are inconsistent with our observed ratio of 4. Other experiments have measured this ratio, yielding values of $\approx 4$ (*Ariel 5*, 2–15 keV) (Watson, Warwick, & Corbet 1982), $\approx 10$ (WATCH/*Granat*, 8–20 keV) (Chichkov et al. 1995), $\approx 20$ (*HEAO 1*, 13–40 keV) (Rothschild & Soong 1987), and 50 (*EXOSAT*, 0.9–21 keV) (Haberl 1991), possibly suggesting changes in the density profile of the wind.

The inability of the radiative wind model to predict the peak at apastron motivated the circumstellar disk model of Pravdo et al. (1995). Although there is no direct observational evidence for a circumstellar disk, recent work by Ignace, Cassinelli, & Bjorkman (1996) has shown that even moderate rotation (like that seen in Wray 977) can lead to formation of an equatorially enhanced wind and perhaps a circumstellar disk.

For simplicity, we assume that the neutron star moves within a circumstellar disk modeled as (Waters et al. 1989)

$$\rho(r) = \rho_0\left(\frac{r}{R_c}\right)^{-n}\,, \tag{8}$$

$$v_{r,w}(r) = v_0\left(\frac{r}{R_c}\right)^{n-2}\,, \tag{9}$$

$$v_{{\rm rot},w}(r) = v_{{\rm rot},c}\left(\frac{r}{R_c}\right)^{-\alpha}\,, \tag{10}$$

where $r$ is the distance from the star, $v_{r,w}$ and $v_{{\rm rot},w}$ are, respectively, radial and rotational components of the wind velocity, and $v_{{\rm rot},c}$ is the rotational velocity of the star. A finite $v_{r,w}$ shifts the location of the accretion peaks and breaks their temporal symmetries. We fix $v_{{\rm rot},w} = 80$ km s$^{-1}$ (allowing for a higher value than the $v \sin i$ measurement) and $\alpha = 1$ (assuming that the disk material conserves angular momentum). The observed periastron/apastron flux ratio then requires $n = 3.7$, within the range of $3 \le n \le 3.75$ derived for six known Be/X-ray binaries (Waters et al. 1988). The symmetrical apastron peak implies $v_0 \lesssim 1$ km s$^{-1}$. Although observations of known Be stars suggest ($2 \lesssim v_0 \lesssim 20$) km s$^{-1}$, its value is largely uncertain (Lamers & Waters 1987). We adopt $v_0 = 0.5$ km s$^{-1}$ in our fit to the folded flux history, which is shown in Figure 12. Pravdo et al. (1995) suggested that if the orbital plane was inclined with respect to that of the disk, then the neutron star may intersect the disk slightly before periastron, resulting in a preperiastron flux peak. However, the dis-

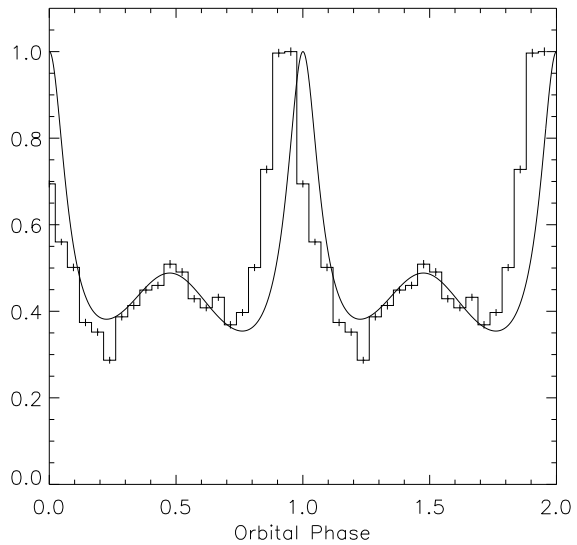


FIG. 12.—A comparison of the folded flux history and the fit obtained using a circumstellar disk model with the following parameters: $v_0 = 0.5$ km s$^{-1}$, $v_{{\rm rot},w} = 80$ km s$^{-1}$, $\alpha = 1$, and $n = 3.7$. Both the fit and the histogram have been normalized by their respective peak values.

placement required to reproduce the observed shift implies a preapastron peak at an orbital phase $\approx 0.3$, which is not observed.

So neither of these accretion models predict the pre-periastron peak of the orbit-folded flux profile, for which many explanations have been proposed. Leahy (1991) and Haberl (1991) suggested that enhanced mass loss from the inner Lagrangian point L1 near periastron would form a gas stream (Stevens 1988) and accrete onto the neutron star prior to periastron. Leahy's model fitted the flux and column density measurements of *Tenma* only at orbital phases $0.75 \lesssim \phi_{\rm orb} \lesssim 1.2$. Haberl's model predicts another flux peak at orbital phase 0.3, when the neutron star intersects the gas stream a second time, which we do not observe. However, we note that the orbital phase of the peak in Haberl's model depends strongly on the shape of the gas stream, which in turn depends on the radial wind velocity profile, a poorly known quantity due to, for example, ionization effects.

Chichkov et al. (1995) suggested that the heating of the stellar wind by the X-rays from the neutron star would reduce the Bondi-Hoyle accretion rate prior to periastron. This occurs when the sound speed of the X-ray–heated gas becomes larger than the relative velocity between the neutron star and the stellar wind. The supply of matter to the neutron star then shuts off prematurely sometime before periastron passage. Another possible source of variability in the Bondi-Hoyle accretion is direct modification of the stellar wind properties by the X-ray heating and ionization (Ho & Arons 1987a, 1987b; Blondin 1994). This has not been investigated in detail for this eccentric system and might yield some new insights.

## 5. CONCLUSIONS

The two rapid spin-up episodes we observed are the most striking features in the spin frequency history of GX $301-2$. The steady spin-up strongly suggests the temporary formation of an accretion disk about the neutron star. Aside from these episodes, there is virtually no net change in the spin frequency of the neutron star on yearly timescales. This suggests that the neutron star accretes primarily from the stellar wind of the companion; if accretion disks form at all, they must alternate generally between prograde and retrograde directions on timescales $\lesssim 4$ days. However, the two spin-up episodes observed (Fig. 6) strongly suggest that a long-lived ($\approx 30$ days) accretion disk with a definite sense of rotation can sometimes form to spin up the neutron star. Since the net change in neutron star spin period in nearly 4 yr of BATSE observations is due almost entirely to the two spin-up episodes, it is possible that the measured decrease in the period of $\approx 25$ s since 1984 (Fig. 1) is entirely due to spin-up episodes similar to the two we have observed, with a recurrence timescale $\approx 2$ yr. This interpretation is also consistent with the secular spin-up rate extrapolated from the previous decade of observations. The pre-1984 frequency history does not exhibit this secular trend, implying that similar spin-up episodes may not have occurred during that era.

In addition to the well-known flux maximum just before periastron passage, the pulsed flux history folded at the orbital period reveals a secondary maximum close to apastron, which is difficult to account for in a spherically symmetric radiative wind. Accretion from a circumstellar disk might explain this phenomena but is by no means unique. It might be profitable to apply the X-ray heating and ionization scenario of Ho & Arons (1987a, 1987b) to this eccentric wind-fed system. A careful consideration of the parameters of the binary system (see Fig. 10) has allowed us to place an upper limit on the mass and radius of the companion, which argues against the reclassification by K95 of the star as a B1 Ia+ hypergiant. More detailed optical observations (particularly a spectral and luminosity classification) of this object would better constrain its mass, radius, and distance.

The question remains as to what causes the formation of the transient accretion disks and what sets their approximately yearly recurrence timescale. We speculated here that formation of these transient disks is related to episodic mass loss from the companion. Simultaneous multiwavelength observations of GX $301-2$ during the next spin-up episode may help answer these questions as well as provide new insights into the mechanism of mass transfer in wind-fed accreting binaries.

We thank Dong Lai for helpful discussions, Colleen Wilson for analyzing occultation data for pulsed fraction determination, and the anonymous referee for insightful comments. This work was funded in part by NASA grants NAG 5-1458 and NAGW-4517. L. B. was supported by Caltech's Lee A. DuBridge Fellowship, funded by the Weingart Foundation and the Alfred P. Sloan Foundation. D. C. was supported by a NASA GSRP Graduate Fellowship under grant NGT-51184. The NASA Compton Postdoctoral Fellowship program has supported L. B. (NAG 5-2666), D. C. (NAG 5-3109), and R. N. (NAG 5-3119).

## APPENDIX A

## TIME-DELAY MEASUREMENTS USING THE CROSS-SPECTRUM TECHNIQUE

The time delay between a pulse template and a folded profile has been found traditionally by maximizing their cross correlation. The statistical error in each phase bin and uncertainty in the cross correlation is easy to find when photon-counting statistics dominate the measurement noise. However, it is not so simple to estimate errors for measurements dominated by a background that varies on a timescale comparable to the signal and has a complicated (i.e., not white) power spectrum.

As demonstrated by Figure 2, the low-frequency noise in BATSE is highly frequency-dependent and much stronger than counting noise. However, the noise is "locally Gaussian" (i.e., Gaussian in all narrow ranges of frequencies). We can thus measure the noise at any frequency, and estimate the shift between template and profile for each harmonic using the cross spectrum (Bendat & Piersol 1986). This allows us to find the statistical errors and construct a minimum-variance estimate of the shift. A technique described by Deeter & Boynton (1986) and Boynton & Deeter (1986) to estimate time delays in

signal-dominated measurements where changes in pulse shape contribute significantly to the uncertainties is almost equivalent.

Each pulse profile is generated by folding a 2 day–long time series at the fundamental pulsar frequency, $f_0$, into $N_b$ bins. Let $x(k)$ and $y(k)$, $0 \leq k < N_b$, denote the zero-meaned template and the profile, respectively. Assuming that the profile is a scaled, shifted version of the template, we can model the profile as

$$y_{\rm mod}(k) = \alpha x(k - \tau_0 N_b/P) , \tag{A1}$$

where $\alpha$ is the scaling factor, $\tau_0$ is the time shift, and $P$ is the epoch-folding period. We then expand $x(k)$ and $y(k)$ in Fourier series and treat the Fourier coefficients as statistically independent. Deeter & Boynton (1986) point out that this is not strictly true in the presence of strong background fluctuations with a long coherence length. The difference in phase between each harmonic of the profile and template is a (nearly) statistically independent measure of the shift between the profile and the template. The phase difference at harmonic $j$ is found using the cross spectrum, $C_j$, defined as the product of the Fourier transform of the template, $X_j$, with the complex conjugate of the Fourier transform of the profile, $Y_j$: $C_j = X_j Y_j^*$. The argument of $C_j$ is the phase difference in the $j$th harmonic. If the profile is a shifted, scaled version of the template, then the phase shift at harmonic $j$, $\phi_j$, is given by

$$\phi_j = \arg (C_j) = 2\pi\tau_0 j/P . \tag{A2}$$

The argument of $C_j$ scales linearly with harmonic number, $j$, and has slope $2\pi\tau_0/P$. We then find the shift, $\tau_0$, by performing a linear least-squares fit to the observed phase differences, $\phi_j$, with $\tau_0$ as the only fit parameter. This is formally equivalent to a weighted average of $\phi_j$ of the form

$$\tau_0 = \left(\frac{P}{2\pi}\right)\left(\sum_{j=1}^{N_b/2} \frac{j\phi_j}{\sigma_j^2}\right)\left(\sum_{j=1}^{N_b/2} \frac{j^2}{\sigma_j^2}\right)^{-1} , \tag{A3}$$

where $\sigma_j^2$ is the variance in the measurement of $\phi_j$. Because it was derived from a least-squares statistic, equation (A3) is a minimum-variance estimate of the shift between profile and template. It remains to estimate $\sigma_j$.

Since the template has much better statistics than the individual profiles, we can measure the phase difference at any harmonic as well as we can measure the phase of the Fourier coefficient of the profile at that harmonic. Determining the uncertainty in the phase shift is equivalent to determining the uncertainty in the phase of a sinusoid. The Fourier transform of the profile at harmonic $j$, $Y_j$, is the sum of the Fourier transform of the signal and the noise at $\nu_j$: $Y_j = Y_j^s + Y_j^n$. The phase of $Y_j$ is given by

$$\arg (Y_j) = \arctan [\mathrm{Im} (Y_j)/\mathrm{Re} (Y_j)] . \tag{A4}$$

The precision with which we can measure phase is independent of phase, and we can assume without loss of generality that the phase of the signal is zero. In that case, $\mathrm{Im} (Y_j^s) = 0$, $\arg (Y_j) \approx \mathrm{Im} (Y_j)/\mathrm{Re} (Y_j)$, and the variance in $\arg (Y_j)$ is given approximately by

$$\mathrm{var} [\arg (Y_j)] \simeq \mathrm{var} [\mathrm{Im} (Y_j^n)]/[\mathrm{Re} (Y_j)]^2 . \tag{A5}$$

Because the noise is locally Gaussian, $\mathrm{var} [\mathrm{Im} (Y_j^n)] = \mathrm{var} (Y_j^n)/2 = P_j^n/2$, where $P_j^n$ is the noise power at $\nu_j$. Thus, the uncertainty in phase is

$$\delta \arg (Y_j) = \left(\frac{P_j^n}{2P_j^s}\right)^{1/2} . \tag{A6}$$

The variance in the $j$th phase shift is simply one-half the ratio of the signal and noise powers at $\nu_j$, both of which we measure from the daily power spectra. Since higher harmonics are dominated by noise, we only used seven harmonics in performing the least-squares fit. Even for $j < 7$, we used only high signal-to-noise harmonics for finding $\tau_0$. To probe the validity of our assumptions, the reduced $\chi^2$ were computed for all the single parameter fits undertaken to measure time delays. The pulse profiles for GX 301−2 are typically detected in approximately three out of the seven harmonics. In the vicinity of periastron passage, the number of harmonics detected increases to $\approx$4–5. For a single parameter fit with three points, the distribution of the reduced $\chi^2$ is expected to be

$$f(\chi^2) = \exp (-\chi^2) . \tag{A7}$$

Figure 13 compares the reduced $\chi^2$ histogram for those 173 fits, which were significant detections at two or more harmonics, with the expected distribution. The same template constructed from 235 two-day folded profiles were used for all the fits. The slight excess of fits with high, reduced $\chi^2$ arise from the increased number of harmonics detected near periastron passage. The agreement between the actual and the expected distribution demonstrates the validity of the assumptions upon which this method is based. In particular, the assumption that all pulse profiles share a common shape seems to have been borne out. We highlight this since it is also an important assumption made in our flux estimates.

## APPENDIX B

## DETERMINATION OF COUNT RATE AND ITS UNCERTAINTY

Let us define $x(j)$, $0 \leq j \leq N_b - 1$, to be a template with $N_b$ phase bins. Since each phase bin has negligible variance, the count rate, $C$, in the template is given by

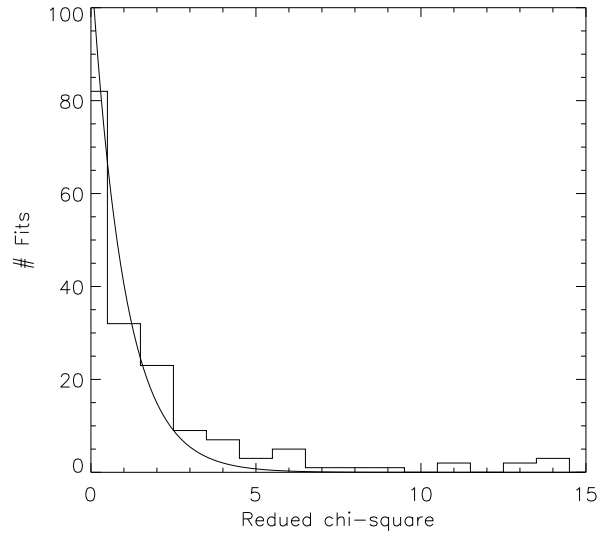


FIG. 13.—The $\chi^2$ histogram for the 173 single-parameter fits performed. The solid line shows the distribution expected for a single-parameter fit with three points. The slight excess of fits with high, reduced $\chi^2$ are due mainly to the increased number of harmonics detected at orbital phases close to periastron passage.

$$C = \frac{1}{N_b} \sum_{j=0}^{N_b - 1} \{x(j) - \min [x(j)]\} . \tag{B1}$$

This equation cannot be used to find the count rate in a typical profile because of the large variance of each phase bin, especially when the signal-to-noise ratio is low. Nevertheless, if the pulse shape of the source is approximately constant, then the count rate of a typical profile can be found by computing the intensity scaling $I$ and the phase $\phi$ that relates the profile and the template amplitudes. The stability of the source pulse shape demonstrated in Appendix A validates the applicability of this technique.

Let us define the complex Fourier amplitudes of the template and profile as $T_j$ and $a_j$, the 1 $\sigma$ uncertainties of the real and imaginary parts of $a_j$ to be $\sigma_j$, the phase shift between the template and the profile to be $\phi$, and the number of harmonics retained in each pulse profile to be $N_h$. Assuming that $a_j$ are independent Gaussian random variables, maximizing

$$\chi^2 = \sum_{j=1}^{N_h} \frac{|a_j - Ie^{ij\phi} T_j|^2}{\sigma_j^2} \tag{B2}$$

dictates the maximum likelihood value of $I$ to be

$$I = \left[ \sum_{j=1}^{N_h} \text{Re} \, (a_j e^{-ij\phi} T_j^*)/\sigma_j^2 \right] \left( \sum_{j=1}^{N_h} |T_j|^2/\sigma_j^2 \right)^{-1} . \tag{B3}$$

Since the profile is assumed to be a scaled version of the template, the most likely value of $\phi$ is that which brings the two in phase. Hence,

$$\arg (a_j e^{-ij\phi} T_j^*) = \arg (a_j) - \arg (e^{ij\phi} T_j) = 0 , \tag{B4}$$

and

$$\text{Re} \, (a_j e^{-ij\phi} T_j^*) = a_j e^{-ij\phi} T_j^* = |a_j| |T_j| . \tag{B5}$$

Substituting this into equation (B3) yields

$$I = \left( \sum_{j=1}^{N_h} |a_j| |T_j|/\sigma_j^2 \right) \left( \sum_{j=1}^{N_h} |T_j|^2/\sigma_j^2 \right)^{-1} , \tag{B6}$$

which we use to find $I$.

The errors in the template amplitudes $T_j$ can be ignored since the template is constructed from 235 pulse profiles. Assuming that noise introduces a Gaussian random deviate into the real and imaginary parts of the measured $a_j$, we write $a_j$ as

$$a_j = a_j^s + n_j , \tag{B7}$$

where $a_j^s$ is the signal component and $n_j$ is the two-dimensional Gaussian noise component. Substituting this into equation (B3) and taking its variance yield

$$\text{var} \, (I) = \left\{ \sum_{j=1}^{N_h} \text{var} \, [\text{Re} \, (n_j e^{-ij\phi} T_j^*)]/\sigma_j^4 \right\} \left( \sum_{j=1}^{N_h} |T_j|^2/\sigma_j^2 \right)^{-2} = \left( \sum_{j=1}^{N_h} |T_j|^2/\sigma_j^2 \right)^{-1} , \tag{B8}$$

which we use to find the errors.

REFERENCES

Bendat, J. S., & Piersol, A. G. 1986, Random Data (New York: Wiley)
Blondin, J. M. 1994, ApJ, 435, 756
Bohm-Vitense, E. 1981, ARA&A, 19, 295
Bord, D. J., Mook, D. E., Petro, L., & Hiltner, W. A. 1976, ApJ, 203, 689
Boynton, P. E., & Deeter, J. E. 1986, in Proc. Inuyama Workshop on the Timing Studies of X-ray Sources, ed. S. Hayakawa & F. Nagase (Nagoya: Nagoya Univ), 13
Castor, J. I., Abbott, D. C., & Klein, R. I. 1975, ApJ, 195, 157
Chakrabarty, D. 1996, Ph.D. thesis, Caltech
Chakrabarty, D., et al. 1993, ApJ, 403, L33
Chichkov, M. A., Syunyaev, R. A., Lund, I. Y., Brandt, S., & Castrotirado, A. 1995, Soviet Astron. Lett., 21, 435
Cox, J. P. 1980, Theory of Stellar Pulsation (Princeton: Princeton Univ. Press)
Deeter, J. E., & Boynton, P. E. 1986, in Proc. Inuyama Workshop on the Timing Studies of X-ray Sources, ed. S. Hayakawa & F. Nagase (Nagoya: Nagoya Univ), 29
Fishman, G. J., et al. 1989, in Proc. of the *GRO* Science Workshop, ed. W. N. Johnson (Greenbelt: NASA/GSFC), 39
Friend, D. B., & Abbott, D. C. 1986, ApJ, 311, 701
Fryxell, B. A., & Taam, R. E. 1988, ApJ, 335, 862
Haberl, F. 1991, ApJ, 376, 245
Hammerschlag-Hensberge, G., Zuiderwijk, E. J., & van den Heuvel, E. P. J. 1976, A&A, 49, 321
Hansen, C. J., & Kawaler, S. D. 1994, Stellar Interiors (New York: Springer)
Harmon, B. A., et al. 1992, in *Compton Observatory* Science Workshop, ed. C. R. Shrader, N. Gehrels, & B. Dennis (CP-3137; Washington, DC: NASA), 69
Ho, C., & Arons, J. 1987a, ApJ, 316, 283
———. 1987b, ApJ, 321, 404
Ignace, R., Cassinelli, J. P., & Bjorkman, J. E. 1996, ApJ, 459, 671
Joss, P. C., & Rappaport, S. A. 1984, ARA&A, 22, 537
Kaper, L., Lamers, H. J. G. L. M., Ruymaekers, E., van den Heuvel, E. P. J., & Zuiderwijk, E. J. 1995, A&A, 300, 446 (K95)
Kumar, P., Ao, C. O., & Quataert, E. J. 1995, ApJ, 449, 294
Lamers, H. J. G. L. M., & Waters, L. B. F. M. 1987, A&A, 182, 80
Leahy, D. A. 1991, MNRAS, 250, 310
Lutovinov, A. A., Grebenev, S. A., Syunyaev, R. A., & Pavlinskii, M. N. 1994, Astron. Lett., 20, 538
Nagase, F. 1989, PASJ, 41, 1
Parkes, G. E., Mason, K. O., Murdin, P. G., & Culhane, J. L. 1980, MNRAS, 191, 547
Pravdo, S. H., Day, C. S. R., Angelini, L., Harmon, B. A., Yoshida, A., & Saraswat, P. 1995, ApJ, 454, 872
Rauw, G., Vreux, J. M., Gosset, E., Hutsemekers, D., Magain, P., & Rochowicz, K. 1996, A&A, 306, 771
Ravenhall, D. G., & Pethick, C. J. 1994, ApJ, 424, 846
Rothschild, R. E., & Soong, Y. 1987, ApJ, 315, 154
Rubin, B. C., Lai, F., Fishman, G. J., Finger, M. H., Harmon, B. A., Paciesas, W. S., Pendleton, G. N., & Wilson, R. B. 1996, A&AS, 121, 687
Sato, N., Nagase, F., Kawai, N., Kelly, R. L., Rappaport, S., & White, N. W. 1986, ApJ, 304, 241 (S86)
Schaller, G., Schaerer, D., & Maeder, G. M. A. 1992, A&AS, 96, 269
Schmidt-Kaler, T. 1982, in Numerical Data and Functional Relationships in Science and Technology, New Series, Vol. 2, Astronomy and Astrophysics, ed. K. Schaifers & H. H. Voigt (Berlin: Springer), 1
Standish, E. M., Newhall, X. X., Williams, J. G., & Yeomans, D. K. 1992, in Explanatory Supplement to the Astronomical Almanac, ed. P. K. Seidelmann (Mill Valley: University Science), 279
Stevens, I. R. 1988, MNRAS, 232, 199
Stothers, R. B., & Chin, C. W. 1995, ApJ, 451, L61
Taam, R. E., & Fryxell, B. A. 1989, ApJ, 339, 297
Waters, L. B. F. M., Demartino, D., Habets, G. M. H. J., & Taylor, A. R. 1989, A&A, 223, 207
Waters, L. B. F. M., Taylor, A. R., van den Heuvel, E. P. J., Habets, G. M. H. J., & Persi, P. 1988, A&A, 198, 200
Watson, M. G., Warwick, R. S., & Corbet, R. H. D. 1982, MNRAS, 199, 915
White, N. E., Mason, K. O., Huckle, H. E., Charles, P. A., & Sanford, P. W. 1976, ApJ, 209, L119
White, N. E., & Swank, J. H. 1984, ApJ, 287, 856